

Generation of fractional and multiple imaginary rotational alignment echoes

Zhenzhong Lian¹, Zhan Hu¹, Hongxia Qi¹, Dehou Fei¹, Sizuo Luo¹, Zhou Chen^{1,*} and Chuan-Cun Shu^{2,†}

¹*Institute of Atomic and Molecular Physics, Advanced Light Field and Modern Medical Treatment Science and Technology Innovation Center of Jilin Province, Jilin University, Changchun 130012, China*

²*Hunan Key Laboratory of Nanophotonics and Devices, Hunan Key Laboratory of Super-Microstructure and Ultrafast Process, School of Physics and Electronics, Central South University, Changsha 410083, China*



(Received 11 May 2021; accepted 26 October 2021; published 9 November 2021)

We present a theoretical investigation to understand the connection between the formation of different rotational alignment echoes and the underlying excitation pathways induced by temporally delayed laser pulses. The fractional and multiple imaginary alignment echoes are predicted and demonstrated in the linear polar molecule carbonyl sulfide. We also use a two-dimensional spectrum obtained from higher-order alignment echo signals to identify the underlying quantum coherence. This work deepens our understanding of the alignment echo phenomenon. It provides a way to gain insight into the relationship between the echo signal and the underlying pathway with potential applications in rotational echo spectroscopy.

DOI: [10.1103/PhysRevA.104.053105](https://doi.org/10.1103/PhysRevA.104.053105)

I. INTRODUCTION

The phenomenon of echo, which causes the signal to return to its origin, has many manifestations in the quantum world [1–4]. The corresponding echo spectroscopy has been widely utilized in many different areas, such as nuclear magnetic resonance [5], high harmonic generation [6], and the electronic and vibrational two-dimensional spectrum [7,8]. Nowadays, control over rotational states and rotational molecular dynamics that leads to field-free molecular alignment and orientation are well developed by using resonant terahertz pulses [9–19] or using nonresonant ultrashort optical pulses [20–24]. Interestingly, the molecular alignment echo (AE) was recently introduced [25] and used to study the relaxation process in dense environments [26–29]. Related studies of other systems and applications have also been reported [30–32]. The observation of AE [33] originated from the study of the nonadiabatic field-free alignment [34–37]. The molecular axis is periodically and preferentially distributed in a specific direction in the spatial space after interacting with the ultrashort pump pulse [38]. A typical AE experiment involves two time-delayed ultrashort pulses, in which the second pulse is applied at a time delay $t = \tau$ to the first one and AE occurs at twice the delay, i.e., $t = 2\tau$, where τ can be shorter than the rotational revival time. The amplitude of the AE signal is sensitive to nonunitary decoherence processes, providing an alternative approach to extract rapid dephasing processes of rotational states in ultrafast timescales. Different kinds of rotational echoes, for example, fractional AE, multiple AE, rotated AE, and imaginary AE (IAE), have also been observed [39–42] and the AE formation is usually explained in the filamented phase space with respect to the angular velocity and polar

angle [25]. Since many rotational states are involved that lead to complex quantum interferences between excitation pathways, the understanding of AE becomes difficult. Recently, the rotational density matrix was used to describe the AE and fractional AE [43,44]. However, it remains challenging to gain insight into the underlying excitation mechanism especially for the counterintuitive IAE phenomenon.

This work will show a combined theoretical and numerical analysis to visualize quantum coherence for the generation of rotational AE and IAE induced by two time-delayed pump pulses. Different kinds of rotational AEs are connected with the rotational excitation processes described by the double-sided Feynman diagram. We predict the existence of the fractional and multiple IAEs and demonstrate these interesting AE phenomena in the linear polar molecule carbonyl sulfide (OCS) by numerically solving the Liouville–von Neumann equation. A two-dimensional (2D) spectrum is calculated to reveal the involved interaction processes. This work provides an alternative way to identify the different echo signals, which will result in potential applications in rotational spectroscopy.

The remainder of this paper is organized as follows. We perform the theoretical analysis for observing AEs and IAEs in Sec. II and present the results of the numerical simulations and discussion in Sec. III. A brief summary is given in Sec. IV.

II. THEORETICAL ANALYSIS

To start our analysis, Fig. 1 illustrates the general concept of observing field-free alignment and different AEs. We consider a standard AE model of molecules in its ground vibronic state with a rotational constant of B , in which the AE is induced by two pulses P_1 and P_2 polarized in the same direction and with a time delay τ . To describe the generation of standard alignment revival signal and then different AEs, the density matrix operator $\hat{\rho}(t)$ is used, which can be expanded

*phy_cz@jlu.edu.cn

†cc.shu@csu.edu.cn

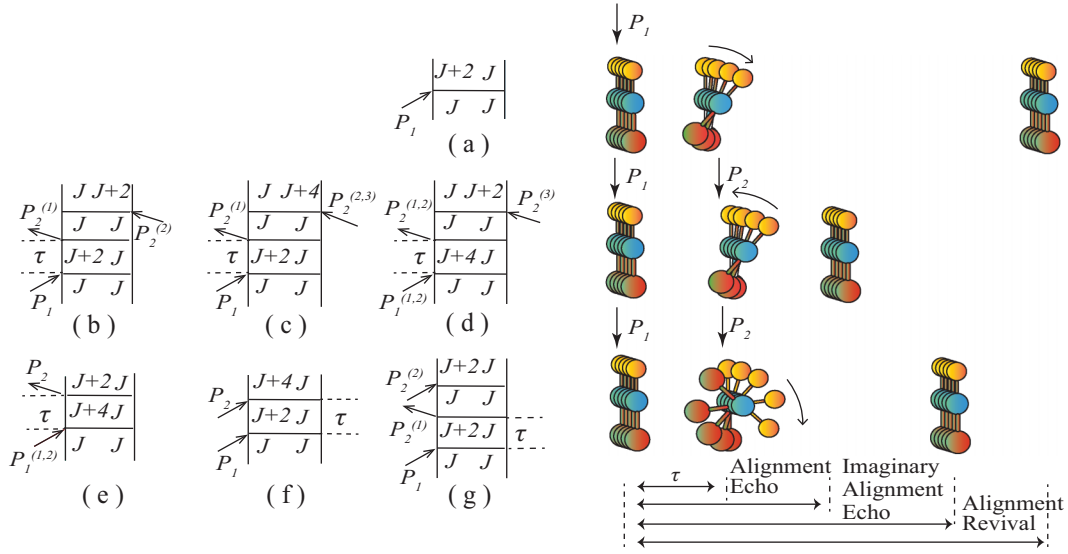


FIG. 1. Schematic of a double-sided Feynman diagram explaining different kinds of alignment signals and the pictorial representations. The first line shows the alignment revival, the second line the normal alignment echo, and the third line the imaginary alignment echo. The arising times of different AEs and IAEs depend on the coherences induced by P_1 and P_2 . (a) Normal alignment. (b) Primary AE. (c) Half fractional AE. (d) Double AE. (e) Double IAE. (f) Half IAE. (g) Primary IAE.

in rotational eigenstates $|JM\rangle$ of a rigid rotor in a field-free space. Since M is conserved under the linearly polarized pump pulse, we omit it for convenience in the following description; therefore, the $\hat{\rho}$ can be described as

$$\hat{\rho}(t) = \sum_{J,J'} \rho_{J,J'} |J\rangle\langle J'|, \quad (1)$$

where $\rho_{J,J'}$ represents the density matrix element of $\hat{\rho}$. The diagonal elements with $J = J'$ give the probability of occupying a rotational state $|J\rangle$ and the off-diagonal ones describe the coherence between the corresponding states $|J\rangle$ and $|J'\rangle$. The rotational eigenstate $|J\rangle$ is governed by the field-free Hamiltonian \hat{H}_0 satisfying $\hat{H}_0|J\rangle = E_J|J\rangle$ with eigenenergies $E_J = BJ(J+1)$.

Figure 1 shows different excitation pathways in Liouville space using double-sided Feynman diagrams starting from an initial population $\rho_{J,J} = |J\rangle\langle J|$ and the pictorial representations of alignment signal, AE, and IAE. The vertical lines on the left and right sides of each diagram represent the ket and bra vector with time evolution upward. The arrows pointing towards (outward) the lines represent the photon absorption (emission) that induces the transition into a higher (lower) state. Raman excitation that happens during the interaction between the femtosecond laser pulse and the rotational states corresponds to a $\Delta J = \pm 2$ transition. This one-step transition is the building block for multiple excitations, through which higher J states can be excited. The simplest Raman excitation process by a single pulse P_1 is shown in Fig. 1(a). After the interaction, the initial state $|J\rangle$ is excited to the higher state $|J+2\rangle$, which generates a two-quantum coherence $|J+2\rangle\langle J|$ between states $|J+2\rangle$ and $|J\rangle$,

$$\rho_{J+2,J}^{(1)}(t) = c_{J+2}^{(1)} c_J^{(1)*} e^{-i\omega_{J+2,J}t}, \quad (2)$$

with $c_J^{(1)}$ the complex coefficient of the eigenstate J after the interaction with P_1 and a beat frequency of $\omega_{J+2,J} = (E_{J+2} -$

$E_J)/\hbar = (4J+6)B/\hbar$. A transient alignment is obtained during the interaction with P_1 . Each state will then freely evolve, inducing a phase of $\omega_{J+2,J}t$ for the coherence $|J+2\rangle\langle J|$. This time-dependent phase determines the revival feature of the nonadiabatic alignment and the echo signals. After a certain period of time T_{rev} , coherences $|J+2\rangle\langle J|$ with different J will become in phase and the transient alignment is revived [45,46]. The expectation value of $\cos^2\theta(t)$, where θ is the angle between the molecular axis and the laser pulse's polarization, is usually used to quantify this field-free alignment behavior

$$\begin{aligned} \langle \cos^2\theta \rangle(t) &= \text{Tr}[\cos^2\theta \hat{\rho}^{(1)}(t)] \\ &= \sum_J \rho_{J+2,J}^{(1)}(t) \langle J+2 | \cos^2\theta | J \rangle + \text{c.c.} \\ &= \sum_J c_{J+2}^{(1)} c_J^{(1)*} e^{-i\omega_{J+2,J}t} \langle J+2 | \cos^2\theta | J \rangle + \text{c.c.} \end{aligned} \quad (3)$$

The coherence between $\Delta J = \pm 2$ contributes to the signal. The diagram beside Fig. 1(a) shows a pictorial representation of the alignment revival. The interaction with P_1 induces a transient alignment of different rotors, after which these rotors start to freely evolve with different frequencies. After a period of T_{rev} , these rotors become in phase again and aligned. When the second pulse P_2 comes with a delay τ , the excitation process becomes more complicated. For the coherence $|J+2\rangle\langle J|$ induced by P_1 as shown in Fig. 1(b), P_2 can lead it to a reverse direction with an opposite beat frequency via two steps of excitation. The superscript of P_1 (P_2) in the diagram represents the number of excitations induced by P_1 (P_2), which is omitted when there is only one step of excitation. The contribution of this process to the density matrix can be described as

$$\rho_{J,J+2}^{(2)}(t) = c_J^{(2)} c_{J+2}^{(2)*} c_{J+2}^{(1)} c_J^{(1)*} e^{-i\omega_{J+2,J}\tau} e^{-i\omega_{J,J+2}t}. \quad (4)$$

Here $c_J^{(2)}$ represents the complex coefficient of state J after the interaction with P_2 . The phase accumulated before the second pulse will then be eliminated after the same time τ , leading the coherence back to the origin where a transient alignment occurs. This corresponds to the primary AE signal

$$\langle \cos^2 \theta \rangle(t) = \sum_J c_J^{(2)} c_{J+2}^{(2)*} c_{J+2}^{(1)} c_J^{(1)*} e^{-i\omega_{J+2,J}\tau} e^{-i\omega_{J,J+2}t} \times \langle J+2 | \cos^2 \theta | J \rangle + \text{c.c.} \quad (5)$$

Pictorially, it can be understood using the picture to the right of Fig. 1(d). After the interaction with P_2 , the rotation direction of each rotor is reversed with the speed unchanged. All the rotors will thus rotate back and become aligned after the same time of τ .

The diagrams shown in Figs. 1(c) and 1(d) also are related to a similar process but with higher excitation orders. As shown in Fig. 1(c), P_2 induces a coherence between $|J\rangle$ and $\langle J+4|$ via three steps of excitation. The beat frequency $\omega_{J,J+4} \sim -8J$ evolves two times quicker than the $|J+2\rangle\langle J|$ induced by P_1 . Thus, the time it takes to cancel out the accumulated phase $\omega_{J,J+4}\tau$ during τ is halved, which corresponds to the half AE. In contrast, when the frequencies induced by P_1 is larger than that of P_1 , the rotating back time for the rotors will become longer, leading to the multiple AEs. Figure 1(d) shows the corresponding excitation process for generating double AE.

Since the time-dependent phase factor determines the arising time of different AE signals, we mainly consider the exponential part. The elimination of the phase accumulated during τ after P_2 can be generally described as

$$0 = \omega_{J_1,J_1'}\tau + \omega_{J_2,J_2'}t, \quad (6)$$

where $\omega_{J_1,J_1'}$ and $\omega_{J_2,J_2'}$ denote the beat frequencies induced after P_1 and P_2 . From the above equation we know that when $t = (-\omega_{J_1,J_1'}/\omega_{J_2,J_2'})\tau$, the phase becomes zero and the alignment echo signal occurs. For different kinds of frequency relation, the signals will occur at different times, corresponding to different kinds of AE signals. We set $N = \omega_{J_1,J_1'}/\omega_{J_2,J_2'}$ hereafter. For primary AE in Fig. 1(b), $N = -1$, the signal is τ after P_2 . The fractional and multiple AEs relate to the situations of $|N| < 1$ and $|N| > 1$.

The IAE, which happens “before” the arrival of the pump pulses, was first observed by Lin *et al.* using photon ionization detection [40]. They observed such a signal τ earlier than the revival signal of P_1 . We can also use the present method to explain the generation of this phenomenon. The third line in Fig. 1 shows the IAE excitation processes. It corresponds to that the new coherence induced by P_2 has inherited the phase but does not change the propagation direction, i.e., $N > 0$. For example, when the first pulse generates the coherence between $|J+4\rangle\langle J|$ as shown in Fig. 1(e), a phase of $\omega_{J+4,J}\tau$ will be accumulated until the arrival of P_2 . After interacting with P_2 , the coherence is transferred into $|J+2\rangle\langle J|$, which has the initial phase of $\omega_{J+4,J}\tau$. As a result, the time it takes for those coherences to become in phase and leading to a transient alignment signal will decrease. The alignment signal relating

to this process can be described as

$$\langle \cos^2 \theta \rangle(t) = \sum_J c_{J+2}^{(2)} c_J^{(2)*} c_{J+4}^{(1)} c_J^{(1)*} e^{-i\omega_{J+4,J}\tau} e^{-i\omega_{J+2,J}t} \times \langle J+2 | \cos^2 \theta | J \rangle + \text{c.c.} \quad (7)$$

The moments at which these signals occur are also closely related to the phase part of the above equation. To understand this mechanism more clearly, a simple equation similar to Eq. (6) is used to consider this relation. We choose P_2 as the reference. Without P_1 , the combination of different coherences induced by P_2 will form a signal at T_{rev} when the coherences become in phase. When the coherence inherits the phase induced by P_1 represented by $\omega_{J_1,J_1'}\tau$, the time for those coherences to become in phase will change to T'_{rev} . The relation between T'_{rev} and τ can be written as

$$\omega_{J_2,J_2'}T'_{rev} = \omega_{J_1,J_1'}\tau + \omega_{J_2,J_2'}T'_{rev}. \quad (8)$$

This implies that the signal will occur at $T'_{rev} = T_{rev} - N\tau$ after P_2 . The T_{rev} in the above equation can also be changed into the half revival or quarter revival period, since there are also certain phase relations at those times, and will lead to an alignment signal. For Fig. 1(e), the beat frequency is halved after interacting with P_2 ; therefore, $N = 2$ and the signal will be 2τ earlier than the revival signal of P_2 and τ earlier than that of P_1 , corresponding to the IAE observed in Ref. [40]. On the other hand, when the beat frequency of the coherence induced by P_2 is larger than that of P_1 as shown in Fig. 1(f), the fractional IAE will arise. In this situation, $N = 1/2$, $T'_{rev} = T_{rev} - \tau/2$, and it will arise between the revival signals of P_2 and P_1 . A pictorial representation of IAE is shown to the right of Fig. 1(g). If angular frequencies of the rotors induced by P_1 become different after the interaction with P_2 , the time it takes for these rotors to become aligned again is changed, which is determined by the relation between $\omega_{J_1,J_1'}$ and $\omega_{J_2,J_2'}$.

It is worth mentioning the situation of $N = 1$, which corresponds to that the coherence does not change after interacting with P_2 as shown in Fig. 1(g). This phenomenon corresponds to the nonrephasing signal in the terahertz rotational spectrum [46] and is different from the situation where the coherence induced by P_1 is not influenced by P_2 at all. The signals generated from these two different processes will co-occur at the revival of P_1 . These two processes compete with each other. By subtracting the signal induced by P_1 alone, these two kinds of signals can be separated. Thus, in the current picture, the primary IAE corresponds to the case of $N = 1$ and the fractional and multiple IAEs correspond to the cases $N < 1$ and $N > 1$, respectively, just like normal AE (“normal” is used sometimes to distinguish from IAE). The IAE observed in Ref. [40] corresponds to the case of $N = 2$, i.e., double IAE.

Based on the above analysis, we can further gain insight into the connection between different kinds of AEs and the underlying excitation pathways. First, since different AEs are closely related to the different excitation process order, fractional and multiple AEs need an intense pump pulse. The intensity ratio between two pump pulses will also affect the intensities of different AEs. Second, there are also fractional and multiple IAEs; the time at which these signals occur concerning the pump delay τ can be determined with Eq. (8). Third, the amplitude of fractional and multiple IAEs should

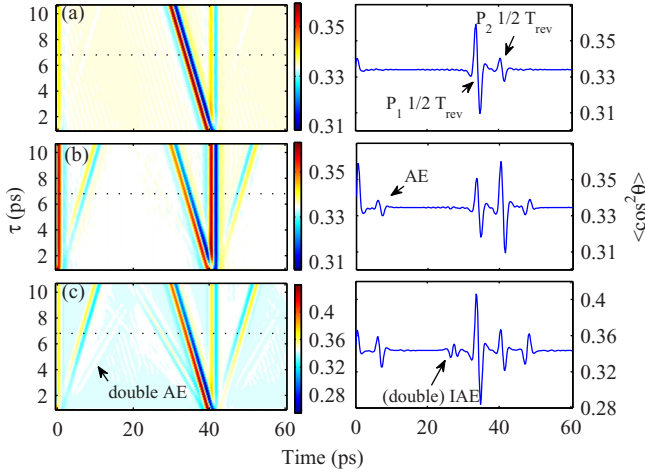


FIG. 2. Shown on the left are the revival signals $\langle \cos^2 \theta(t) \rangle$ of OCS induced by different intensity combinations of two pump pulses with τ varying from 1 to 10.6 ps. On the right is the alignment signal at $\tau = 7$ ps extracted from the left. Different kinds of alignment signals are depicted. (a) $\mathcal{E}_1 = 4 \times 10^9$ V/m and $\mathcal{E}_2 = 2 \times 10^9$ V/m. (b) $\mathcal{E}_1 = 4 \times 10^9$ V/m and $\mathcal{E}_2 = 4 \times 10^9$ V/m. (c) $\mathcal{E}_1 = 8 \times 10^9$ V/m and $\mathcal{E}_2 = 4 \times 10^9$ V/m.

be stronger than the corresponding normal AE with the same $|N|$ since it requires no direction inverse and fewer steps of excitation.

III. RESULTS AND DISCUSSION

To demonstrate the above analysis, we use OCS as a sample, which has a relatively long revival period of 80 ps without a quarter revival signal and therefore is suitable for observing different AE signals. The time-dependent density matrix operator is obtained by numerically propagating the Liouville–von Neumann equation with the total Hamiltonian of the system $\hat{H}(t) = \hat{H}_0 - \hat{V}(t)$ with $\hat{V}(t) = \frac{1}{2} \Delta \alpha \cos^2 \theta \varepsilon^2(t)$, where $\Delta \alpha$ denotes the polarizability anisotropy and $\varepsilon(t)$ is the total electric field of the laser pulses [38]. In our simulations, we take two Gaussian profile transform-limited pulses with a duration of 90 fs and the strengths of electric fields \mathcal{E}_1 and \mathcal{E}_2 for the pulses P_1 and P_2 . The degree of molecular alignment $\langle \cos^2 \theta \rangle(t)$ and higher-order rotational signal $\langle \cos^4 \theta \rangle(t)$ are calculated by considering a weighted average of the alignment signals emanating from all of the different initial states. In our simulations, the initial thermal temperature is set at 50 K by including the Boltzmann distribution of 30 initial J states. The results of a continuous change of τ are calculated, from which the relation between the arising time of the AE signal and τ can be clearly revealed. The centrifugal distortion and dephasing are not taken into account in the simulation. To examine the effect of the pump field intensities on the primary AEs, Fig. 2 shows the results of three different combinations of \mathcal{E}_1 and \mathcal{E}_2 . We calculate the revival signal $\langle \cos^2 \theta \rangle(t)$ of OCS with τ ranging from 1 to 10.6 ps. The false colormaps on the left present the overall revival signal for τ and the evolution time after P_2 . We set the arriving time of P_2 as zero. Since the AE signals also periodically arise and have fractional revival,

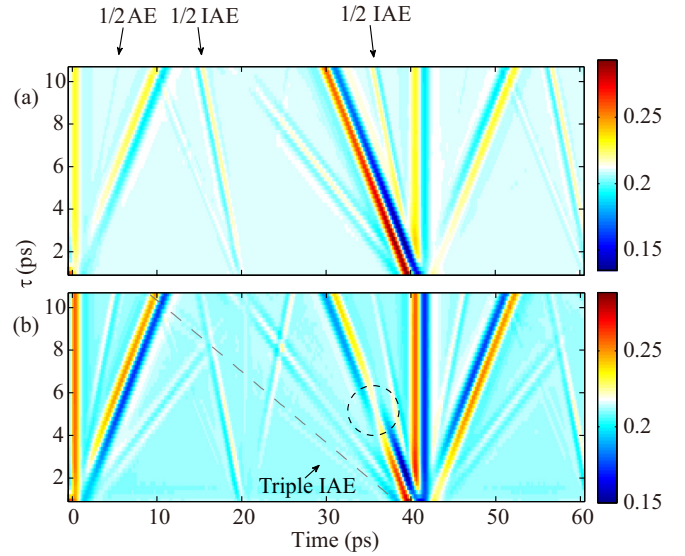


FIG. 3. Higher-order signal $\langle \cos^4 \theta \rangle(t)$ of OCS induced by the same \mathcal{E}_1 of 8×10^9 V/m and different \mathcal{E}_2 of (a) 4×10^9 V/m and (b) 6×10^9 V/m. The signals corresponding to half AE, half IAE, and triple IAE are labeled.

a free evolution time of 60 ps, which is about 3/4 of the OCS revival time, is long enough to see all the signals. The revival signal of $\tau = 7$ ps extracted from each false colormap is shown on the right. Figure 2(a) shows the revival signals with $\mathcal{E}_1 = 4 \times 10^9$ V/m and $\mathcal{E}_2 = 2 \times 10^9$ V/m. As can be seen, the half revival signals induced by P_1 and P_2 dominate. We can barely see any other signal. However, when we increase \mathcal{E}_2 to the same value as \mathcal{E}_1 , a clear echo signal, which occurs τ after the second pulse, appears as shown in Fig. 2(b). We further increase \mathcal{E}_1 to 8×10^9 V/m while keeping \mathcal{E}_2 unchanged. The double AE and IAE emerge as shown in Fig. 2(c). Also, the primary AE intensity increases compared to Fig. 2(b). From the different choice of pump intensities, the dependence of different AEs on the excitation processes can be revealed. More information about the dependence of the primary AE on the accurate pump field intensity has been discussed in Ref. [43].

The generation of fractional AE, which comes from more excitation steps with P_2 , requires even higher P_2 intensity than the primary AE. Since higher coherence is induced after P_2 , the expectation of higher power $\langle \cos^{2n} \theta \rangle(t)$, with integer $n > 1$, will be required to observe such a signal, which can be obtained by measuring high-order harmonic generation in the experiment [39,41]. We calculate $\langle \cos^4 \theta \rangle(t)$ to observe the half AE and the predicted half IAE of OCS. The results of two different \mathcal{E}_2 of 4×10^9 and 6×10^9 V/m with the same \mathcal{E}_1 of 8×10^9 V/m are shown in Figs. 3(a) and 3(b), respectively. From Fig. 3(a) we can see a weak signal labeled with 1/2 AE at $\tau/2$ after the zero points with a slope of 2, which corresponds to the half AE. This half AE signal becomes stronger in Fig. 3(b) with a higher \mathcal{E}_2 , revealing its intensity dependence. As we discussed above, the half IAE also exists and its signal is greater than that of the half AE. We can see that there are signals around $T_{\text{rev}}/4$ and $T_{\text{rev}}/2$ with

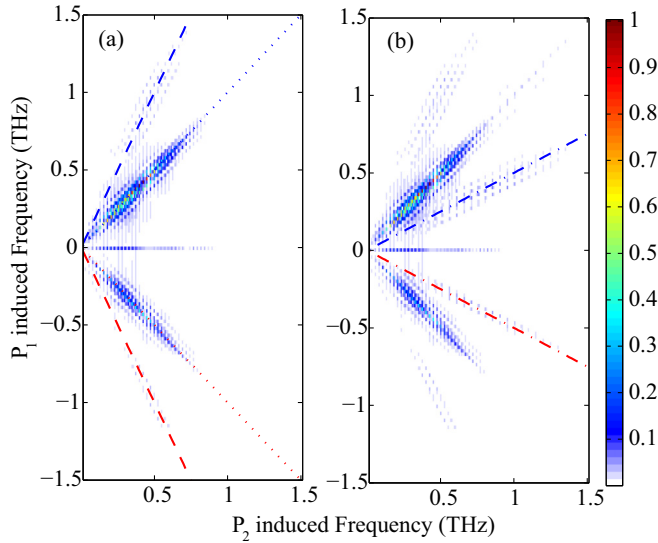


FIG. 4. The 2D Fourier spectrum obtained from (a) the alignment signal $\langle \cos^2 \theta \rangle(t)$ and (b) the higher-order signal $\langle \cos^4 \theta \rangle(t)$ of OCS. Different AE signals are related to certain areas in the spectrum. Blue (red) dashed, dotted, and dash-dotted lines show double, primary, and half IAE (AE), respectively.

a negative slope of 2 labeled with 1/2 IAE in Figs. 3(a) and 3(b). These signals occur at $T_{rev}/4 - \tau/2$ and $T_{rev}/2 - \tau/2$, coincident with the relation presented by Eq. (8) with $N = 1/2$, and correspond to the half IAE. As also can be seen, the amplitude of the half IAE is larger than that of the half AE. However, the intensity dependence of the fractional IAE still needs further discussion. We can also see the weak triple IAE, which has a negative slope of 1/3 in Fig. 3(b) guided by a gray dashed line. There is an interesting flip of the signal in Fig. 3(b) marked using a dashed circle as τ increases from 4 to 6 ps. This indicates that different kinds of signals exist at this time, which can be the revival signal of P_1 or the primary IAE discussed above. The shapes of these two signals are not the same. The increase of one of them will reduce the other. This relation between the two signals, which is related to the pump field intensities and the delay τ , causes the signal to flip.

The above results presented a general relation between the pump intensity and the AE signal and confirmed fractional and multiple IAEs. However, the underlying processes are much more complex due to the multilevel involved and the interference between the adjacent pathways. The intensities of different kinds of AE signals are also affected by the interference process [43,44]. A 2D rotational Fourier spectrum obtained from the Fourier transform of the time-dependent AE signals is used to understand the relationship between the AE and the underlying rotational excitation processes. The resonant 2D terahertz spectrum for rotational states has already been achieved by Lu *et al.* [46] Figure 4 shows the 2D Fourier spectra of the signals $\langle \cos^2 \theta \rangle(t, \tau)$ and $\langle \cos^4 \theta \rangle(t, \tau)$, which have been calculated for relatively long periods of t and τ . The spectra are obtained by a 2D Fourier transform with respect to each delay after subtracting the revival signal

induced by each pulse alone. The intensities of P_1 and P_2 are the same as in Fig. 3(b). Since the echo signals periodically appear as τ varies, as indicated in Eqs. (5) and (7), the Fourier transform of the signal with respect to t and τ can reflect the frequencies ω_{J_1, J'_1} and ω_{J_2, J'_2} induced by P_1 and P_2 , respectively. Meanwhile, as discussed in Sec. II, different AE signals come from different relations between ω_{J_1, J'_1} and ω_{J_2, J'_2} , which will correspond to different parts in the spectrum. The 2D spectrum therefore can reveal the coherence induced by each pulse, providing a way to identify the underlying rotational excitation pathways.

According to the beat frequency relation presented above, the normal AE signal comes from a reverse of the P_1 and P_2 induced frequencies. Thus it relates to the lower quadrant in the spectrum shown in Figs. 4(a) and 4(b), where IAE relates to the upper quadrant. As shown in Fig. 4(a), there are two areas for each quadrant. The diagonal peaks, depicted with dotted lines, relate to the same value of beat frequency induced by two pump pulses, which correspond to the processes that generate the primary AE and IAE. These two processes dominate the spectrum. The areas guided by the dashed line have $|N| \sim 2$ and therefore correspond to the double AE and IAE. We can also see that the signal of IAE is larger than that of AE, which proves that the process relating to the IAE happens more easily than that relating to the normal AE with the same order. There are also peaks among different areas, which correspond to the certain excitation pathway with respect to different J . The intensity of each peak can reflect the possibility of a certain transition, which influences the interference between the corresponding pathways. Figure 4(b) shows the spectrum obtained from the signal $\langle \cos^4 \theta \rangle(t, \tau)$. As can be seen, besides the information contained in Fig. 4(a), there are also areas with $|N| \sim 1/2$, corresponding to the half AE and IAE. Thus the higher-order signal provides more information about the underlying excitation pathways. This is a step forward in completely identifying different pathways of the excitation process. With the 2D spectrum obtained from higher-order signals, more information about the pathways can be identified.

Besides identifying the excitation pathways, the intensity of different peaks in the spectrum reflects the probability of certain excitation. When different pump intensities are adopted, the spectrum will show the emergence and disappearance of different excitation pathways. A continuous changing of the pump intensities may lead to a full visualization of the rotational excitations.

IV. CONCLUSION

We have examined the generation of alignment echo signals with different excitation processes and predicted the existence of multiple and fractional imaginary alignment echoes. Based on theoretical analysis, we observed all kinds of alignment echo signals using the nonadiabatic excitation of carbonyl sulfide with different combinations of pump pulse intensities. A higher-order two-dimensional spectrum was calculated to identify the involved quantum coherence between states. This work provides a simple approach to visualize the connection between rotational excitation processes and

the corresponding coherence signals. The results can deepen the understanding of the alignment echo generation and its relation to quantum revival signals.

ACKNOWLEDGMENT

This work was supported by the National Natural Science Foundation of China under Grants No. 12074143, No. 12104177, and No. 61973317.

-
- [1] E. L. Hahn, *Phys. Rev.* **80**, 580 (1950).
- [2] N. A. Kurnit, I. D. Abella, and S. R. Hartmann, *Phys. Rev. Lett.* **13**, 567 (1964).
- [3] J. H. Malmberg, C. B. Wharton, R. W. Gould, and T. M. O’Neil, *Phys. Rev. Lett.* **20**, 95 (1968).
- [4] M. Herrera, T. M. Antonsen, E. Ott, and S. Fishman, *Phys. Rev. A* **86**, 023613 (2012).
- [5] R. Damadian, *Science* **171**, 1151 (1971).
- [6] G. Stupakov, *Phys. Rev. Lett.* **102**, 074801 (2009).
- [7] F. D. Fuller and J. P. Ogilvie, *Annu. Rev. Phys. Chem.* **66**, 667 (2015).
- [8] D. M. Jonas, *Annu. Rev. Phys. Chem.* **54**, 425 (2003).
- [9] A. Goban, S. Minemoto, and H. Sakai, *Phys. Rev. Lett.* **101**, 013001 (2008).
- [10] O. Ghafur, A. Rouzée, A. Gijsbertsen, W. K. Siu, S. Stolte, and M. J. J. Vrakking, *Nat. Phys.* **5**, 289 (2009).
- [11] S. Fleischer, Y. Zhou, R. W. Field, and K. A. Nelson, *Phys. Rev. Lett.* **107**, 163603 (2011).
- [12] S. Fleischer, R. W. Field, and K. A. Nelson, *Phys. Rev. Lett.* **109**, 123603 (2012).
- [13] K. Nakajima, H. Abe, and Y. Ohtsuki, *J. Phys. Chem. A* **116**, 11219 (2012).
- [14] C.-C. Shu and N. E. Henriksen, *Phys. Rev. A* **87**, 013408 (2013).
- [15] K. N. Egodapitiya, S. Li, and R. R. Jones, *Phys. Rev. Lett.* **112**, 103002 (2014).
- [16] K. Lin, I. Tutunnikov, J. Qiang, J. Ma, Q. Song, Q. Ji, W. Zhang, H. Li, F. Sun, X. Gong, H. Li, P. Lu, H. Zeng, Y. Prior, I. S. Averbukh, and J. Wu, *Nat. Commun.* **9**, 5134 (2018).
- [17] L. Xu, I. Tutunnikov, E. Gershnel, Y. Prior, and I. S. Averbukh, *Phys. Rev. Lett.* **125**, 013201 (2020).
- [18] C.-C. Shu, Q.-Q. Hong, Y. Guo, and N. E. Henriksen, *Phys. Rev. A* **102**, 063124 (2020).
- [19] Q.-Q. Hong, L.-B. Fan, C.-C. Shu, and N. E. Henriksen, *Phys. Rev. A* **104**, 013108 (2021).
- [20] K. F. Lee, D. M. Villeneuve, P. B. Corkum, A. Stolow, and J. G. Underwood, *Phys. Rev. Lett.* **97**, 173001 (2006).
- [21] T. Suzuki, Y. Sugawara, S. Minemoto, and H. Sakai, *Phys. Rev. Lett.* **100**, 033603 (2008).
- [22] R. Damari, S. Kallush, and S. Fleischer, *Phys. Rev. Lett.* **117**, 103001 (2016).
- [23] E. T. Karamatskos, S. Raabe, T. Mullins, A. Trabattoni, P. Stammer, G. Goldsztejn, R. R. Johansen, K. Długołeckı, H. Stapelfeldt, M. J. J. Vrakking, S. Trippel, A. Rouzée, and J. Küpper, *Nat. Commun.* **10**, 3364 (2019).
- [24] Z. Lian, H. Qi, J. Li, J. Bo, J. Deng, X. Liu, S. Luo, S.-y. Li, D. Fei, Z. Chen, and Z. Hu, *J. Phys. Chem. A* **125**, 770 (2021).
- [25] G. Karras, E. Hertz, F. Billard, B. Lavorel, J.-M. Hartmann, O. Faucher, E. Gershnel, Y. Prior, and I. S. Averbukh, *Phys. Rev. Lett.* **114**, 153601 (2015).
- [26] H. Zhang, B. Lavorel, F. Billard, J. M. Hartmann, E. Hertz, O. Faucher, J. Ma, J. Wu, E. Gershnel, Y. Prior, and I. S. Averbukh, *Phys. Rev. Lett.* **122**, 193401 (2019).
- [27] J. Ma, H. Zhang, B. Lavorel, F. Billard, E. Hertz, J. Wu, C. Boulet, J.-M. Hartmann, and O. Faucher, *Nat. Commun.* **10**, 5780 (2019).
- [28] J.-M. Hartmann, J. Ma, T. Delahaye, F. Billard, E. Hertz, J. Wu, B. Lavorel, C. Boulet, and O. Faucher, *Phys. Rev. Research* **2**, 023247 (2020).
- [29] J. Ma, H. Zhang, B. Lavorel, F. Billard, J. Wu, C. Boulet, J.-M. Hartmann, and O. Faucher, *Phys. Rev. A* **101**, 043417 (2020).
- [30] D. Rosenberg and S. Fleischer, *Phys. Rev. Research* **2**, 023351 (2020).
- [31] J. Qiang, I. Tutunnikov, P. Lu, K. Lin, W. Zhang, F. Sun, Y. Silberberg, Y. Prior, I. S. Averbukh, and J. Wu, *Nat. Phys.* **16**, 328 (2020).
- [32] I. Tutunnikov, K. V. Rajitha, and I. S. Averbukh, *Phys. Rev. A* **103**, 013717 (2021).
- [33] H. Jiang, C. Wu, H. Zhang, H. Jiang, H. Yang, and Q. Gong, *Opt. Express* **18**, 8990 (2010).
- [34] T. Seideman, *Phys. Rev. Lett.* **83**, 4971 (1999).
- [35] Y. Ohshima and H. Hasegawa, *Int. Rev. Phys. Chem.* **29**, 619 (2010).
- [36] S. Fleischer, Y. Khodorkovsky, E. Gershnel, Y. Prior, and I. S. Averbukh, *Isr. J. Chem.* **52**, 414 (2012).
- [37] C. P. Koch, M. Lemesko, and D. Sugny, *Rev. Mod. Phys.* **91**, 035005 (2019).
- [38] H. Stapelfeldt and T. Seideman, *Rev. Mod. Phys.* **75**, 543 (2003).
- [39] G. Karras, E. Hertz, F. Billard, B. Lavorel, G. Siour, J. M. Hartmann, O. Faucher, E. Gershnel, Y. Prior, and I. S. Averbukh, *Phys. Rev. A* **94**, 033404 (2016).
- [40] K. Lin, P. Lu, J. Ma, X. Gong, Q. Song, Q. Ji, W. Zhang, H. Zeng, J. Wu, G. Karras, G. Siour, J.-M. Hartmann, O. Faucher, E. Gershnel, Y. Prior, and I. S. Averbukh, *Phys. Rev. X* **6**, 041056 (2016).
- [41] B. Wang, L. He, Y. He, Y. Zhang, R. Shao, P. Lan, and P. Lu, *Opt. Express* **27**, 30172 (2019).
- [42] L. Xu, I. Tutunnikov, L. Zhou, K. Lin, J. Qiang, P. Lu, Y. Prior, I. S. Averbukh, and J. Wu, *Phys. Rev. A* **102**, 043116 (2020).
- [43] D. Rosenberg, R. Damari, and S. Fleischer, *Phys. Rev. Lett.* **121**, 234101 (2018).
- [44] P. Wang, L. He, Y. He, S. Sun, R. Liu, B. Wang, P. Lan, and P. Lu, *Opt. Express* **29**, 663 (2021).
- [45] D. Rosenberg, R. Damari, S. Kallush, and S. Fleischer, *J. Phys. Chem. Lett.* **8**, 5128 (2017).
- [46] J. Lu, Y. Zhang, H. Y. Hwang, B. K. Ofori-Okai, S. Fleischer, and K. A. Nelson, *Proc. Natl. Acad. Sci. USA* **113**, 11800 (2016).